

# Journal of Materials Chemistry A

Accepted Manuscript



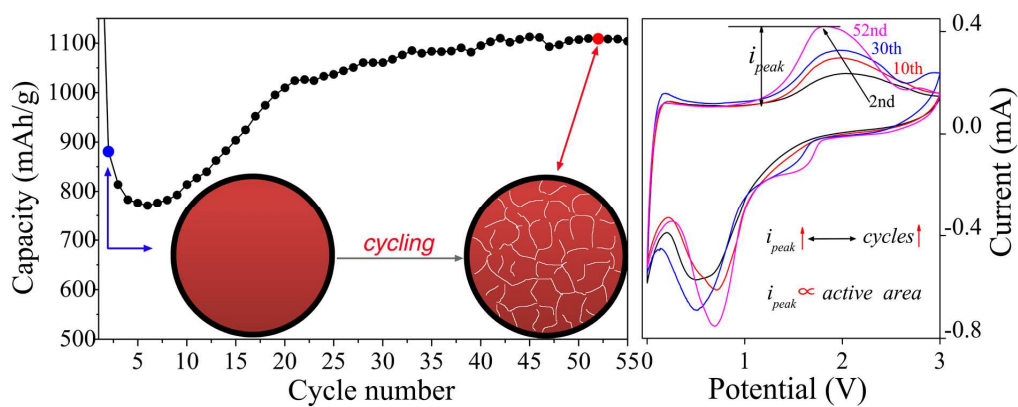
This is an *Accepted Manuscript*, which has been through the Royal Society of Chemistry peer review process and has been accepted for publication.

*Accepted Manuscripts* are published online shortly after acceptance, before technical editing, formatting and proof reading. Using this free service, authors can make their results available to the community, in citable form, before we publish the edited article. We will replace this *Accepted Manuscript* with the edited and formatted *Advance Article* as soon as it is available.

You can find more information about *Accepted Manuscripts* in the [Information for Authors](#).

Please note that technical editing may introduce minor changes to the text and/or graphics, which may alter content. The journal's standard [Terms & Conditions](#) and the [Ethical guidelines](#) still apply. In no event shall the Royal Society of Chemistry be held responsible for any errors or omissions in this *Accepted Manuscript* or any consequences arising from the use of any information it contains.

## Graphical Abstract



The  $\gamma\text{-Fe}_2\text{O}_3\text{/C/MWNT}$  electrode activates via the vesiculation of  $\gamma\text{-Fe}_2\text{O}_3\text{/C}$  nanoparticles, leading to improved reversible capacity.

# Electrode Activation via Vesiculation: Improved Reversible Capacity of $\gamma$ -Fe<sub>2</sub>O<sub>3</sub>@C/MWNT Composite Anode for Lithium-ion Batteries

Yongfei Liu,<sup>\*a</sup> Junmin Xu,<sup>b</sup> Xiaoying Qin,<sup>\*a</sup> Hongxing Xin,<sup>a</sup> Xueqin Yuan,<sup>a</sup> Jian Zhang,<sup>a</sup> Di Li<sup>a</sup> and Chunjun Song<sup>a</sup>

Capacity fading caused by pulverization is the basic issue for transition-metal-oxide anodes in lithium-ion batteries (LIBs). Here we report a simple and scalable fabrication of core-shell structured  $\gamma$ -Fe<sub>2</sub>O<sub>3</sub>@C nanoparticle based composites incorporated with multi-walled carbon nanotube (MWNTs), through a vacuum-carbonization of the synthesized metal-organic complex and MWNT hybrids. In the constructed  $\gamma$ -Fe<sub>2</sub>O<sub>3</sub>@C/MWNT architectures, the carbon shell layers can not only buffer the volume change of  $\gamma$ -Fe<sub>2</sub>O<sub>3</sub> nanoparticles but also improve their conductivity; while the flexible and conductive MWNT networks can maintain the structural and electrical integrity of the electrodes during the charge/discharge cycles. As a result, such  $\gamma$ -Fe<sub>2</sub>O<sub>3</sub>@C/MWNT electrodes, as tested as anodes for LIBs, exhibit excellent cycling performance with monotonically increased reversible capacities along with cycles. For instance, the specific capacity rises at a rate of  $\sim 6.8$  mAh/g per cycle to 1139 mAh/g after 60 cycles at the current density of 100 mA/g. Such electrode activation was revealed to be closely related to the increased active surface area of the electrode arising from the gradually vesiculation in Fe<sub>2</sub>O<sub>3</sub>@C nanoparticles during the lithiation/delithiation in the as-prepared robust  $\gamma$ -Fe<sub>2</sub>O<sub>3</sub>@C/MWNT architectures.

## Introduction

Rechargeable lithium-ion batteries (LIBs) are increasingly used for portable electronics, electric vehicles, and other applications.<sup>1-4</sup> Since the commercial graphite anode material has already approached its theoretical limit (372 mAh/g),<sup>5</sup> it is urgent nowadays to seek alternative anode materials with a high reversible capacity and a long life-time. In this context, Fe<sub>2</sub>O<sub>3</sub>-based materials have emerged as promising candidates for next generation LIB anodes because of their high theoretical capacity (1007 mAh/g), low cost, and environmental acceptance. However, Fe<sub>2</sub>O<sub>3</sub> electrodes suffer from poor electrical conductivity and poor cycle performance with large capacity fading because of pulverization caused by the drastic volume change during charge-discharge process,<sup>6, 7</sup> which hinder its practical applications for LIBs. Several strategies have been proposed to overcome these drawbacks and further enhance the structural stability for the Fe<sub>2</sub>O<sub>3</sub>-based materials. One approach is to increase the effective contact area between

the active materials and the electrolyte by designing nanostructure and hierarchical micro/nanostructures, or controlling pore structures, such as using  $\alpha$ -Fe<sub>2</sub>O<sub>3</sub> nanoflakes,<sup>8</sup>  $\alpha$ -Fe<sub>2</sub>O<sub>3</sub> nanorods,<sup>9</sup> Fe<sub>2</sub>O<sub>3</sub> microboxes,<sup>10</sup> spindle-like mesoporous  $\alpha$ -Fe<sub>2</sub>O<sub>3</sub> particles,<sup>11</sup> which can reduce the path lengths for the transport of electrons and lithium ions. Another approach is to use hybrid electrodes composed of Fe<sub>2</sub>O<sub>3</sub> and carbon materials, such as single-walled carbon nanohorns/ $\alpha$ -Fe<sub>2</sub>O<sub>3</sub> composites,<sup>12</sup> reduced graphene oxide/Fe<sub>2</sub>O<sub>3</sub> composite,<sup>13</sup> and Fe<sub>2</sub>O<sub>3</sub>-CNT-graphene hybrid materials,<sup>14</sup> which can effectively improve the conductivity and fast charge/discharge rates of the electrodes. Meanwhile, these carbon materials can also accommodate the mechanical strain of lithium ion insertion/extraction much better than the bare Fe<sub>2</sub>O<sub>3</sub> electrode materials. These strategies inspire us to rationally design and synthesize an anode material system with unique structures to enhance their electrochemical performance.

As we know, the capacity of lithium storage for Fe<sub>2</sub>O<sub>3</sub> anodes is mainly achieved through the reversible conversion

reaction between  $\text{Li}^+$  and  $\text{Fe}_2\text{O}_3$  active materials.<sup>8</sup> Recent studies have noticed that interfacial lithium storage generally takes place as a result of the electrochemical reaction at the interface of active materials, in which a gradually increased capacity exhibits during the initial several cycles.<sup>11,15</sup> However, the detailed activation mechanism involved is not yet fully understood,<sup>15</sup> and the relationship between electrode activation and microstructure evolution with cycles has also not been deeply studied. On the other hand, although  $\alpha\text{-Fe}_2\text{O}_3$  materials have been widely investigated as anodes for LIBs nowadays,<sup>8-17</sup> only a few studies were performed on the electrochemical performance of  $\gamma\text{-Fe}_2\text{O}_3$  anode materials.<sup>18,19</sup> Lee et al. fabricated  $\gamma\text{-Fe}_2\text{O}_3$ /carbon microparticles through a hydrothermal method followed by the chemical vapor deposition. They obtained a specific capacity of 900 mAh/g after 40 cycles at 100 mA/g when tested as an anode.<sup>18</sup> Vargas and co-workers reported the hydrothermal synthesis of  $\gamma\text{-Fe}_2\text{O}_3$ /graphene nanosheets composite, which retained a reversible capacity of 429 mAh/g after 100 cycles at 1000 mA/g.<sup>19</sup> Very recently, Natelson's group showed that a composite material made of graphene nanoribbons and  $\gamma\text{-Fe}_2\text{O}_3$  nanoparticles could exhibit a high discharge capacity of ~910 mAh/g after 134 cycles at 100 mA/g.<sup>20</sup> Despite the progress achieved to date, the researches on the facile and scalable synthesis of  $\gamma\text{-Fe}_2\text{O}_3$ -based materials with a high specific capacity and a long life-time are still in very early stage.

Herein, we report the fabrication of core-shell structured  $\gamma\text{-Fe}_2\text{O}_3$ @C nanoparticle based composites incorporated with multi-walled carbon nanotubes (MWNTs). When tested as anodes for LIBs, such  $\gamma\text{-Fe}_2\text{O}_3$ @C/MWNT electrodes exhibit excellent cycling performance and monotonically elevated reversible capacity. For instance, its capacity rises at a rate of ~6.8 mAh/g per cycle to 1139 mAh/g after 60 cycles, as the charge/discharge current density is equal to 100 mA/g; or its capacity rises at a rate of ~2.0 mAh/g per cycle to 723 mAh/g after 200 cycles at the current density of 1000 mA/g. By *ex situ* high-resolution transmission electron microscopy (HRTEM) examinations, we show that the core-shell structured  $\gamma\text{-Fe}_2\text{O}_3$ @C nanoparticles transform into vesiculate structure without pulverization during the cyclic charge/discharge. As the vesiculate structure develops, the core-shell structured  $\gamma\text{-Fe}_2\text{O}_3$ @C/MWNT anodes are gradually activated. It was revealed that the activation of the electrode is closely related to the increase of active surface area arising from the gradual formation of vesiculate structure.

## Experimental

### Synthesis of $\gamma\text{-Fe}_2\text{O}_3$ @C/MWNT Composite

The reagents were obtained from commercial sources and used without further purification. The  $\gamma\text{-Fe}_2\text{O}_3$ @C/MWNT composite was synthesized through a carbonization of the hybrid of metal-organic complexes and MWNTs. Typically, terephthalic acid (PTA, 3.99 g),  $\text{LiOH}\cdot\text{H}_2\text{O}$  (2.01 g), and MWNTs (0.63 g) were dissolved and dispersed in 500 mL of warm ionized water (60 °C) with supersonic treatment for 30 min. Then 6.66 g of  $\text{FeSO}_4\cdot 7\text{H}_2\text{O}$  was added into the mixed solution with stirring for 24 h to form the hybrid of ferrous benzoate and MWNTs. After filtering the as-prepared precursors were vacuum sealed in a quartz tube and calcined at 500 °C for 4 h. Then the obtained powders were further annealed at 200 °C for 24 h in the air to form the  $\gamma\text{-Fe}_2\text{O}_3$ @C/MWNT composites (Fig. 1a). For comparison, core-

shell structured  $\gamma\text{-Fe}_2\text{O}_3$ @C nanoparticles were also prepared in the absence of MWNTs.

### Characterizations

Scanning electron microscopy (SEM) investigations were conducted on a FEI Sirion 200 field emission SEM. TEM and HRTEM experiments were performed on a JEOL JEM-2010 TEM. Powder X-ray diffraction (XRD) was conducted on a Panalytical X'Pert Pro MPD X-ray diffractometer using  $\text{Cu K}\alpha$  radiation ( $\lambda = 1.54 \text{ \AA}$ ). X-ray photoelectron spectroscopy (XPS) analysis was conducted on VG ESCALAB Mark II X-ray photoelectron spectroscope. Thermogravimetric analysis (TGA) analysis was conducted on a Perkin-Elmer Pyris 1 thermal gravimetric analyzer at a heating rate of 10 °C/min from 25 °C to 700 °C in air flow.

### Battery Fabrication and Electrochemical Measurement

The electrodes were made through a standard procedure as following: active materials ( $\gamma\text{-Fe}_2\text{O}_3$ @C/MWNT and  $\gamma\text{-Fe}_2\text{O}_3$ @C composites), super-P carbon black, and polyvinylidene fluoride (PVDF), in a weight ratio of 7:2:1 were blended in N-methylpyrrolidone (NMP) to form a homogenous slurry. Electrodes were prepared by coating the slurry on a copper foil and then vacuum-dried at 120 °C for 12 h. Standard CR2032 coin cells were assembled in an Ar-filled glove box, using lithium foil as the counter electrode, 1 M  $\text{LiPF}_6$  in ethylene carbonate/dimethyl carbonate/diethyl carbonate (1:1:1 by volume) as the electrolyte, and Celgard 2325 as the separator. Cyclic voltammetry (CV) measurement was conducted at 0.2 mV/s in the range of 0~3.0 V on a CHI660C electrochemical workstation. The electrochemical impedance spectroscopy (EIS) of the cells were evaluated in the frequency range from 0.01 Hz to 100 kHz at Zahner Zennium electrochemistry work station. Discharge-charge measurements of the cells were performed between the potential range of 0.01~3.0 V (vs.  $\text{Li/Li}^+$ ) under a Neware BTS TC53 battery test system. All of the specific capacities were calculated on the basis of the total weight of the  $\gamma\text{-Fe}_2\text{O}_3$ @C/MWNT or  $\gamma\text{-Fe}_2\text{O}_3$ @C composites.

## Results and discussion

As shown in Fig. 1a, the synthetic protocol of the  $\gamma\text{-Fe}_2\text{O}_3$ @C/MWNT composite is mainly composed of two steps. First, the ferrous benzoate and MWNTs composites were synthesized by a modified procedure based on the reported work.<sup>21</sup> In this synthesis, the introduced  $\text{LiOH}\cdot\text{H}_2\text{O}$  provided an alkaline condition to dissolve PTA into the ionized water, which facilitated the next reaction. In the second step, after a vacuum annealing, the as-prepared ferrous benzoate precursor was converted to  $\gamma\text{-Fe}_2\text{O}_3$  nanoparticles capsulated by carbon layer, while the MWNT network still remained, thus leading to the formation of  $\gamma\text{-Fe}_2\text{O}_3$ @C/MWNT composites.

Fig. 1b shows a typical SEM image of the as-prepared  $\gamma\text{-Fe}_2\text{O}_3$ @C/MWNT composites. Evidently, a large number of dispersed particles with ~100 nm in size are distributed homogeneously in the 3D MWNT networks. The corresponding TEM images reveal that these nanoparticles are composed of agglomerated nanograins with sizes ranging from ~10 to 50 nm and entangled with MWNT networks (Fig. 1c), and the carbon shell layer encapsulating around the core is ~3 nm in thickness (Fig. 1d). It should be emphasized that the addition of MWNTs in the synthesis is favorable to form a robust hybrid

nanoarchitectures, but does not affect the formation of core-shell structured  $\gamma$ -Fe<sub>2</sub>O<sub>3</sub>@C nanoparticles, which can also form in the absence of MWNTs (see Electronic Supplementary Information Fig. S1a-c†).

XRD patterns of the samples are shown in Fig. 2a. All the peaks of the Fe<sub>2</sub>O<sub>3</sub>@C powders can be indexed to  $\gamma$ -Fe<sub>2</sub>O<sub>3</sub> with a cubic phase (JCPDS card No. 39-1346). No obvious peaks of carbon were detected, indicating the amorphous attribute of the carbon shell layer. In comparison, the XRD pattern of the  $\gamma$ -Fe<sub>2</sub>O<sub>3</sub>@C/MWNT shows an additional peak at 26°, which can be attributed to the (002) plane of graphitic structure contributed from the MWNTs. HRTEM images of the  $\gamma$ -Fe<sub>2</sub>O<sub>3</sub>@C nanoparticle clearly demonstrate that the  $\gamma$ -Fe<sub>2</sub>O<sub>3</sub> nanoparticle is highly crystallized and the carbon shell presents amorphous state (see Fig. S1c†), highly in agreement with the XRD result. The lattice fringe images (see Fig. S1c, d†) reveal the clear core interfringe distance of 0.48 nm and nanotube interfringe distance of 0.33 nm, which are in good agreement with that of the (111) plane of  $\gamma$ -Fe<sub>2</sub>O<sub>3</sub> and the (002) plane of MWNTs, respectively.

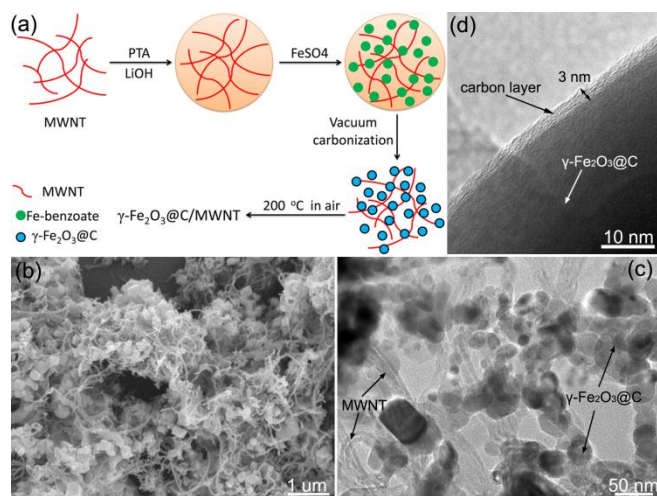


**Fig. 1.** (a) Schematic illustration of the preparation of  $\gamma$ -Fe<sub>2</sub>O<sub>3</sub>@C/MWNT. (b) SEM and (c) TEM images of  $\gamma$ -Fe<sub>2</sub>O<sub>3</sub>@C/MWNT. (d) TEM image of a  $\gamma$ -Fe<sub>2</sub>O<sub>3</sub>@C particle.

In order to further confirm that the synthesized iron oxide cores are maghemite ( $\gamma$ -Fe<sub>2</sub>O<sub>3</sub>), an XPS examination was performed. The typical survey spectrum shows the presence of Fe, C, and O elements in the  $\gamma$ -Fe<sub>2</sub>O<sub>3</sub>@C/MWNT composite (Fig. 2b). The high-resolution spectrum of Fe reveals that, in contrast to Fe<sub>3</sub>O<sub>4</sub> XPS spectrum, it contains the charge transfer satellites of Fe2p<sub>3/2</sub> and Fe2p<sub>1/2</sub> at 720 eV and 732 eV, respectively, which indicate the absence of Fe<sup>2+</sup>, confirming that the core is maghemite ( $\gamma$ -Fe<sub>2</sub>O<sub>3</sub>).<sup>22, 23</sup> Furthermore, TGA was used to reveal the precise chemical composition of the composites (as shown in Fig. 2d). The results show that  $\gamma$ -Fe<sub>2</sub>O<sub>3</sub>@C nanoparticles have a chemical composition of 79 wt %  $\gamma$ -Fe<sub>2</sub>O<sub>3</sub> and 21 wt % C, and the  $\gamma$ -Fe<sub>2</sub>O<sub>3</sub>@C/MWNT composites have a chemical composition of 59 wt %  $\gamma$ -Fe<sub>2</sub>O<sub>3</sub>, 15.7 wt % C, and 25.3 wt % MWNTs (basing on the consideration that the ratio of  $\gamma$ -Fe<sub>2</sub>O<sub>3</sub> to carbon layer is unchanged).

To measure the electrochemical performance of the as-prepared composites, CR2032 coin cells were fabricated according to a widely reported procedure.<sup>24, 25</sup> Their charge storage behaviors were first characterized by cyclic voltammetry (CV). Fig. S2a† shows the representative CV

curves of the  $\gamma$ -Fe<sub>2</sub>O<sub>3</sub>@C electrode at room temperature between 0 and 3.0 V at a scan rate of 0.2 mV/s. In the first discharge cycle, a well-defined cathodic peak at 0.44 V can be observed clearly, which is usually ascribed to the formation of solid electrolyte interphase (SEI) layer and the complete reduction of Fe<sub>2</sub>O<sub>3</sub> to Fe.<sup>25</sup> This peak disappears in the subsequent cycles, while three weak peaks at 0.78, 0.96, and 1.2 V appear, indicating the occurrence of an irreversible phase transformation during the lithiation/delithiation process in the first cycle.<sup>8, 16</sup> During the charge process, a broad anodic peak composed of two peaks (at 1.68 and 1.96 V) are observed, corresponding to the oxidative reactions of Fe<sup>0</sup> to Fe<sup>2+</sup> and Fe<sup>2+</sup> to Fe<sup>3+</sup>, respectively, highly in accord with the electrochemical process of  $\alpha$ -Fe<sub>2</sub>O<sub>3</sub>-based anodes.<sup>17, 26</sup> The  $\gamma$ -Fe<sub>2</sub>O<sub>3</sub>@C/MWNT composite shows similar CV characteristics (see Fig. S2b†).

As shown in Fig. 3a and b, the charge/discharge profiles for the  $\gamma$ -Fe<sub>2</sub>O<sub>3</sub>@C and  $\gamma$ -Fe<sub>2</sub>O<sub>3</sub>@C/MWNT electrodes are also very similar. A potential plateau appears at ~0.75 V during the first discharge process, which represents the reduction of Fe<sub>2</sub>O<sub>3</sub> to form nano-sized Fe<sup>0</sup> and amorphous Li<sub>2</sub>O matrix.<sup>8</sup> The initial discharge and charge capacities are 1091 and 666 mAh/g for  $\gamma$ -Fe<sub>2</sub>O<sub>3</sub>@C, and 1523 and 857 mAh/g for  $\gamma$ -Fe<sub>2</sub>O<sub>3</sub>@C/MWNT, corresponding to irreversible capacity losses of ~39% and ~43%, respectively. Such high capacity loss may be ascribed to the inevitable formation of SEI layer and decomposition of electrolyte, which is usually observed in the Fe-based anode materials.<sup>11</sup> This characteristic is also in agreement with the CV results that the intense cathodic peak at 0.44 V existed in the first scan is absent afterward (see Fig. S2†). The discharge voltage plateau at ~0.75 V in the first cycle is different from those in other cycles afterward at ~1.0 V (Fig. 3a, b), further indicating that irreversible reactions occurred in the first cycle.<sup>26</sup>

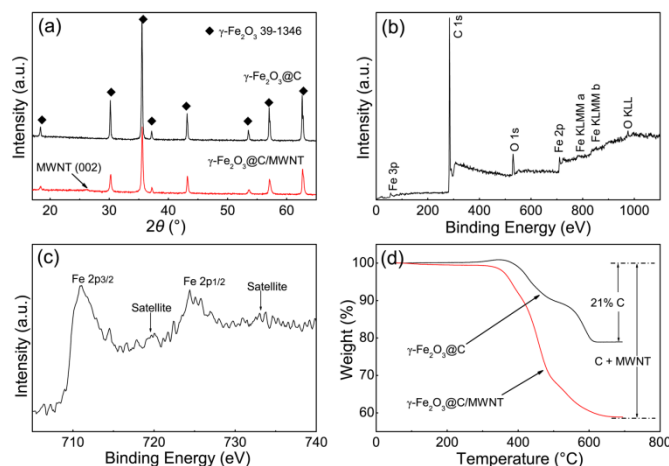


**Fig. 2.** (a) XRD patterns of the composites; (b) and (c) XPS spectra for  $\gamma$ -Fe<sub>2</sub>O<sub>3</sub>@C/MWNT composite; (d) TG curves of the composites.

The cycling performances of the two electrodes are shown in Fig. 3c at a current density of 100 mA/g from 3.0 to 0.01 V. The core-shell structured  $\gamma$ -Fe<sub>2</sub>O<sub>3</sub>@C nanoparticle electrode demonstrates a gradually increased discharge capacity up to 906 mAh/g after 50 cycles. While the as-prepared  $\gamma$ -Fe<sub>2</sub>O<sub>3</sub>@C/MWNT composite electrode delivers higher discharge capacities, increasing at a rate of ~6.8 mAh/g per cycle to 1139 mAh/g after 60 cycles, much higher than that of  $\gamma$ -Fe<sub>2</sub>O<sub>3</sub>@C electrode, indicating a significant enhancement in cycling performance due to the introduction of MWNTs. This

value is also higher than the theoretical capacity of  $\gamma\text{-Fe}_2\text{O}_3$  (1007 mAh/g), such high capacity should be ascribed to the interfacial (surface) Li storage via a pseudo-capacitive mechanism.<sup>27-29</sup> The Coulombic efficiencies for the  $\gamma\text{-Fe}_2\text{O}_3\text{/C/MWNT}$  electrode rapidly increase from 56.3% for the first cycle to about 99% after ten cycles and remains over 97% thereafter (as shown in Fig. 3c), which suggests a facile lithium insertion/extraction.<sup>30</sup> In order to further confirm the advantages of this  $\gamma\text{-Fe}_2\text{O}_3\text{/C/MWNT}$  composites in lithium storage, the capacities of the two electrodes have been investigated upon 200 cycles at the rate of 1000 mA/g and the cycling performances are displayed in Fig. 3d. Thirteen cycles were first performed at 200 mA/g and then 187 cycles at 1000 mA/g. One can see that the reversible capacity for  $\gamma\text{-Fe}_2\text{O}_3\text{/C}$  electrode first rises to 400 mAh/g within 65 cycles and then decreases to 265 mAh/g at the 200th cycle, while that for the  $\gamma\text{-Fe}_2\text{O}_3\text{/C/MWNT}$  electrode rises steadily at a rate of  $\sim 2.0$  mAh/g per cycle from the initial 350 mAh/g to 723 mAh/g after 200 cycles. In addition, the electrochemical performance of pure MWNTs is also examined for comparison. As shown in Fig. S3†, one can find that the specific discharge capacities of the MWNTs decrease gradually during the initial several cycles

and then stabilize at about 200 mAh/g. This is much lower than the reversible capacities of the  $\gamma\text{-Fe}_2\text{O}_3\text{/C}$  electrode, indicating that the capacity enhancement ( $\gamma\text{-Fe}_2\text{O}_3\text{/C}$  vs  $\gamma\text{-Fe}_2\text{O}_3\text{/C/MWNT}$ , as shown in Fig. 3c, d) is due to the synergistic effect of  $\gamma\text{-Fe}_2\text{O}_3\text{/C}$  nanoparticles and MWNTs. The superior cycling stability for the  $\gamma\text{-Fe}_2\text{O}_3\text{/C/MWNT}$  electrode should be attributed to the flexible and conductive MWNTs. One can see that lots of cracks exist in the cycled  $\gamma\text{-Fe}_2\text{O}_3\text{/C}$  anode, while no obvious cracks can be observed in the cycled  $\gamma\text{-Fe}_2\text{O}_3\text{/C/MWNT}$  anode (see Fig. S4†). This result indicates that the addition of MWNTs can not only accommodate the mechanical stress induced by the volume change of the  $\gamma\text{-Fe}_2\text{O}_3\text{/C}$  nanoparticles, but also inhibit the breakdown of electrical connection of the  $\gamma\text{-Fe}_2\text{O}_3\text{/C}$  nanoparticles from the anode and thus maintain the structural and electrical integrity of the electrode during the cyclic charge/discharge processes. Such cycling stability at low and high charge/discharge rate are significantly higher than previously reported works on carbon coated porous  $\gamma\text{-Fe}_2\text{O}_3$  microparticles (900 mAh/g after 40 cycles at 100 mA/g)<sup>18</sup> and  $\gamma\text{-Fe}_2\text{O}_3\text{/graphene}$  nanosheets composite (429 mAh/g after 100 cycles at 1000 mA/g).<sup>19</sup>

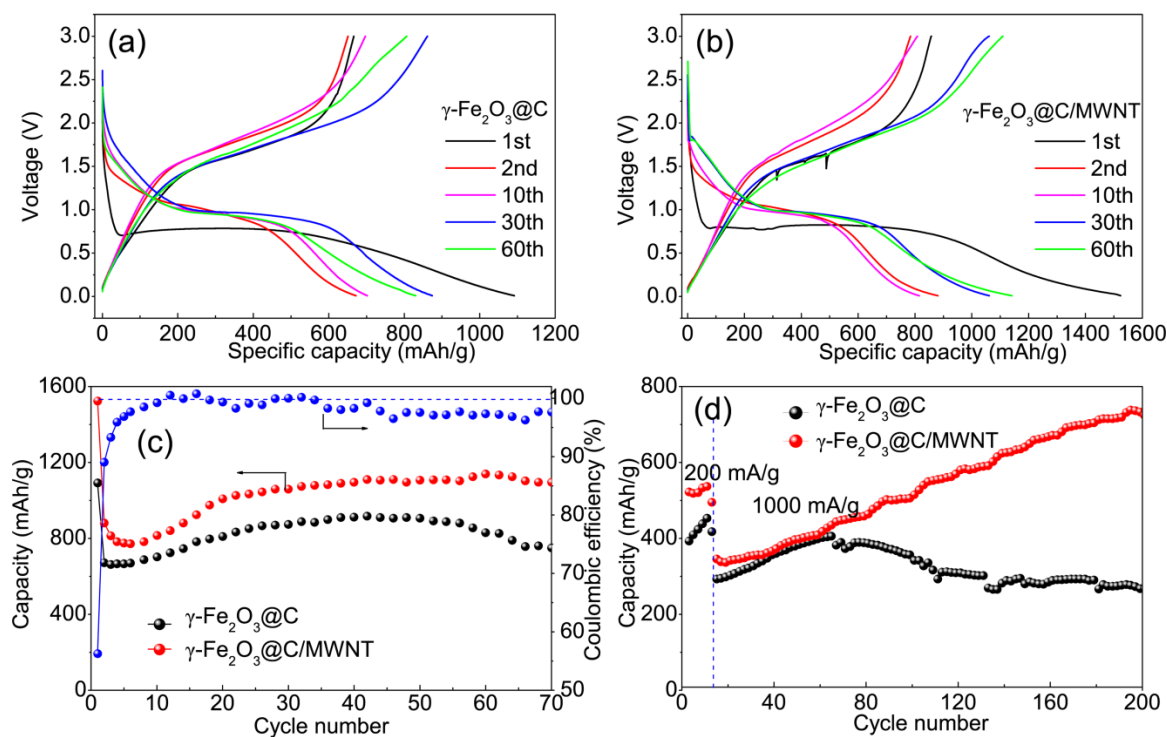


**Fig. 3.** Charge/discharge voltage curves of (a)  $\gamma\text{-Fe}_2\text{O}_3\text{/C}$  and (b)  $\gamma\text{-Fe}_2\text{O}_3\text{/C/MWNT}$  electrodes at a current density of 100 mA/g. Cycling performances and Coulombic efficiencies of the electrodes at the current densities of (c) 100 mA/g and (d) 1000 mA/g.

It is noteworthy that both of the two electrodes show increased capacities at different current densities during the first dozens even hundreds of cycles, implying a gradual activation of the electrodes. Similar phenomenon was also reported for the bare  $\alpha\text{-Fe}_2\text{O}_3$  electrode, which exhibited a discharge capacity rise ( $\sim 6\%$ ) during the initial several cycles.<sup>11</sup> It was ascribed to the reversible formation of a gel-like layer generated from the electrolyte decomposition or further interfacial lithium storage as a result of electrochemical reaction at the interface of active materials.<sup>11, 15, 31</sup> However, for our  $\gamma\text{-Fe}_2\text{O}_3\text{/C/MWNT}$  electrode, the percentages of the increase of the capacity are up to  $\sim 48\%$  (from 770 to 1139 mAh/g at the current density of 100

mA/g) and  $\sim 106\%$  (from 350 to 723 mAh/g at the current density of 1000 mA/g), respectively, which are not common in the reported various nanostructured metal oxide electrodes.<sup>7, 32-36</sup>

To clarify the mechanism of this activation of the electrodes, the CV test was performed for a  $\gamma\text{-Fe}_2\text{O}_3\text{/C/MWNT}$  electrode after different cycles at 100 mA/g. As shown in Fig. 4a, one can see that the intensity of the anodic peak ( $i_{pa}$ ) at  $\sim 1.8$  V and the integral area of the curve (corresponding to the capacity) rise gradually along with the charge/discharge cycles, suggesting that the electrode has been gradually activated and forms a more stable structure, which is capable of withstanding the

volume change. According to Randles-Sevcik equation,<sup>37</sup> the peak current can be described as following:

$$i_{pa} = (2.69 \times 10^5) n^{3/2} A C D^{1/2} v^{1/2} \quad (1)$$

Where  $n$  is the electron stoichiometry during the oxidation/redox reaction,  $A$  is the active surface area of the electrode,  $C$  is the concentration of the diffusing species,  $D$  is the diffusion coefficient of  $\text{Li}^+$ , and  $v$  is the voltage scan rate. For our solid state  $\gamma\text{-Fe}_2\text{O}_3/\text{C}/\text{MWNT}$  electrodes, the  $n$  value is constant during the cycles, and the  $C$  value can also be considered to be unchanged due to the excess of solid lithium counter electrode. Hence, the rise of  $i_{pa}$  indicates a gradual increase of  $A$  and/or  $D$  along with the charge/discharge cycles, which should be closely related to the microstructure evolution of the active materials.

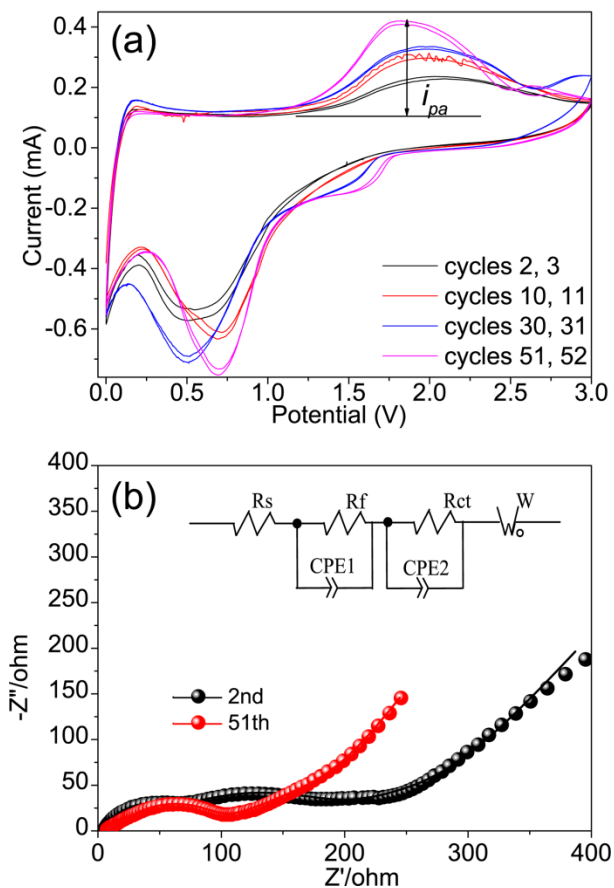


**Fig. 4.** (a) Representative CV curves of a  $\gamma\text{-Fe}_2\text{O}_3/\text{C}/\text{MWNT}$  electrode after different cycles and (b) Nyquist plots ( $Z'$  vs.  $-Z''$ ) of the 2nd and 51st cycles of the  $\gamma\text{-Fe}_2\text{O}_3/\text{C}/\text{MWNT}$  electrode. Symbols represent experimental data and continuous lines represent fitted data using the equivalent electrical circuit of the inset of (b).

In this context, *ex situ* TEM and HRTEM analyses of the electrodes were performed to examine their structural changes along with the cycles (Fig. 5). During the initial several cycles (Fig. 5a-c), the TEM images show that the dense  $\text{Fe}_2\text{O}_3$  nanoparticles have progressively transformed to vesiculate structure, which should originate from the aggregation of the vacancies produced during the extraction of Li, as revealed in the dealloying for Li-alloying anodes.<sup>38-40</sup> The HRTEM image reveals that the  $\text{Fe}_2\text{O}_3$  particle still possesses a relatively integrated microstructure with distinct lattice fringe (Fig. 5e).

After 50 cycles, the  $\text{Fe}_2\text{O}_3$  particles become more loose and porous due to the formation of larger pores at the expense of small pores (Fig. 5d). The corresponding HRTEM image as revealed in Fig. 5f indicates that the  $\text{Fe}_2\text{O}_3$  nanoparticle has transformed to clusters composed of some small nano-domains with almost common crystallographic orientation. Hence, one can conclude that considerable interface including the surfaces of the pores and the interface within the clusters form after the cyclic charge/discharge, which are active sites for the further interfacial lithium storage.<sup>11, 15, 41</sup> Meanwhile, in contrast with the well crystallized zones in the  $\text{Fe}_2\text{O}_3$  nanoparticles, the formed vesiculate structure and the interface (the domain boundaries with the clusters) can also serve as the tunnel for  $\text{Li}^+$  transport, leading a faster diffusion of Li ions. As a result, both the active surface area and the diffusion coefficient increase, highly in agreement with the CV analyses (Fig. 4a). It is worth noting that although the vesiculate structure forms, no pulverization is observed from the TEM investigation, which should be due to the protection of the capsulated carbon shell around the  $\text{Fe}_2\text{O}_3$  nanoparticles.<sup>5, 26</sup> This vesiculate mesoporous structure can provide a large number of interfaces for the interfacial Li storage, leading to a high reversible capacity (1139 mAh/g, as shown in Fig. 3c) beyond the theoretical capacity.

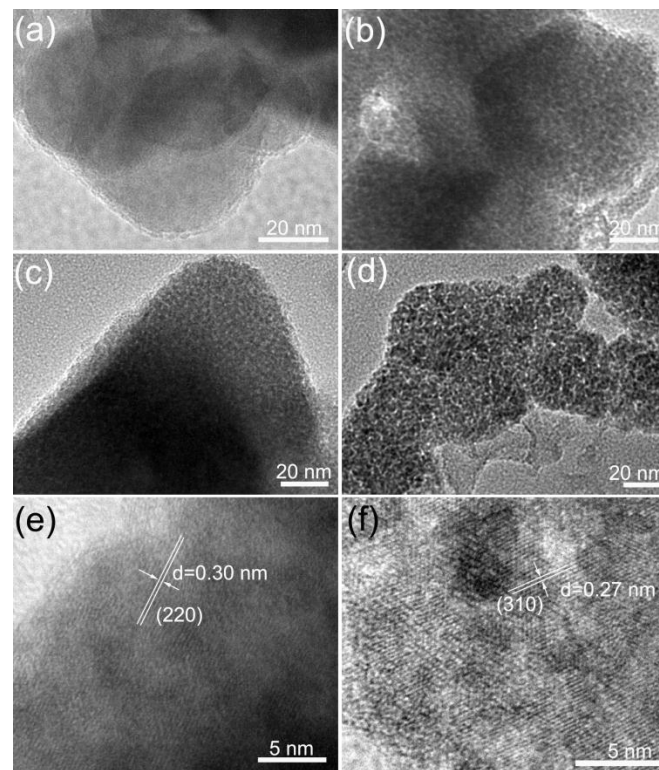


**Fig. 5.** TEM and HRTEM images showing the structure evolution of the  $\gamma\text{-Fe}_2\text{O}_3/\text{C}$  particles with the lithiation/delithiation cycles: (a) 0 cycle, (b) 1 cycle, (c, e) 5 cycles, and (d, f) 50 cycles. All of the cycled electrodes are sampled from the cells in fully charged status. A vesiculate structure of the  $\gamma\text{-Fe}_2\text{O}_3/\text{C}$  particle was gradually formed during the cycles. The interplanar distances of the selected areas are calculated to be 0.30 and 0.27 nm, which agree with the (220) and (310) planes of  $\gamma\text{-Fe}_2\text{O}_3$ , respectively.

**Table 1.** Impedance parameters of the cell, with  $\gamma$ -Fe<sub>2</sub>O<sub>3</sub>@C/MWNT as the cathode and a Li-metal anode, during the 2nd and 51st discharge-charge cycles at ~1.0 V.

parameter	R <sub>s</sub> /Ohm	R <sub>f</sub> /Ohm	R <sub>ct</sub> /Ohm
2 <sup>nd</sup> cycle	3.6	45.9	123.2
51 <sup>st</sup> cycle	5.1	33.1	50.9

Furthermore, electrochemical impedance spectroscopy (EIS) was conducted at frequencies from 100 kHz to 0.01 Hz to understand the effect of the structure evolution of the active materials on their electrochemical performances. The EIS data was analysed by fitting to an equivalent electrical circuit shown in the inset of Fig. 4b. It consists of the electrolyte ( $R_s$ ), surface film ( $R_f$ ), and charge transfer ( $R_{ct}$ ) resistances, two constant phase elements ( $CPE_1$  and  $CPE_2$ ), and a diffusional component Warburg impedance ( $W$ ). As shown in Fig. 4b, the Nyquist plots for the 2nd and 51st cycles are similar, exhibiting a high-frequency depressed semicircle (corresponding to  $R_f$ ) and a medium-frequency depressed semicircle (corresponding to  $R_{ct}$ ) followed by a linear tail (corresponding to  $W$ ) in the low-frequency region.<sup>42</sup> The resistance values after curve fitting are listed in Table 1. One can see that the  $R_f$  of 51st cycle is significantly lower than that of the 2nd cycle. Generally, the increased active surface area upon cycling may lead to the increasing SEI layer, and thus increase the  $R_f$ . However, for our core-shell structured  $\gamma$ -Fe<sub>2</sub>O<sub>3</sub>@C material, the SEI layer formed in the first cycle will shield the vesiculate electrode from the erosion of the electrolyte during the next cycles. In other words, despite the increased active surface area within the  $\gamma$ -Fe<sub>2</sub>O<sub>3</sub>@C nanoparticle upon cycling, no extra SEI layer forms within the  $\gamma$ -Fe<sub>2</sub>O<sub>3</sub>@C nanoparticles. Hence, the  $R_f$  would not increase, but will slightly decrease due to the partial decomposition of the outer SEI layer,<sup>41</sup> leading to the decrease of  $R_f$ . The change of Rct from 123.2 to 50.9  $\Omega$  suggests a significant reduce of charge transfer resistance after cycling, which should be attributed to the formation of the vesiculate structure. The increase of the active surface area arising from such a structure evolution of the electrode can lead to rapid electron transport during the electrochemical lithium insertion/extraction reaction, and thus result in significant improvement on the cycling performance. This result suggests that it is effective to improve the electrochemical performance of metal oxides through the electrode vesiculation.

## Conclusions

In summary,  $\gamma$ -Fe<sub>2</sub>O<sub>3</sub>@C/MWNT nanocomposites have been successfully fabricated by a facile and scalable synthesis method in combination with a vacuum-carbonization process. The  $\gamma$ -Fe<sub>2</sub>O<sub>3</sub>@C/MWNT electrodes deliver increased specific capacities along with cycles, which is closely related to the increased effective active surface area and the porous structure during the vesiculation of the electrode, and the robust structure composed of 3D MWNT networks and  $\gamma$ -Fe<sub>2</sub>O<sub>3</sub>@C nanoparticles. Considering the low cost, environmental acceptance, and large-scale production of the  $\gamma$ -Fe<sub>2</sub>O<sub>3</sub>@C/MWNT in the present work, such anode materials hold great potential for practical applications for lithium ion batteries.

## Acknowledgements

This work was supported in part by National Natural Science Foundation of China (NO. 11374306, NO. 11174292, NO. 50972146, and NO. 10904144).

## Notes and references

<sup>a</sup> Key Laboratory of Materials Physics, Institute of Solid State Physics, Chinese Academy of Sciences, Hefei 230031, P R China. Email: log1218@163.com, xyqin@issp.ac.cn

<sup>b</sup> High Magnetic Field Laboratory, Chinese Academy of Sciences, Hefei 230031, China.

† Electronic Supplementary Information (ESI) available: Experimental details and characterization: Fig. S1–S4. See DOI: 10.1039/b000000x/

- X. Li, X. Meng, J. Liu, D. Geng, Y. Zhang, M. N. Banis, Y. Li, J. Yang, R. Li, X. Sun, M. Cai and M. W. Verbrugge, *Adv. Funct. Mater.*, 2012, **22**, 1647-1654.
- X. Li, A. Dhanabalan, L. Gu and C. Wang, *Adv. Energy Mater.*, 2012, **2**, 238-244.
- Y. Zhao, X. Li, B. Yan, D. Li, S. Lawes and X. Sun, *J Power Sources*, 2015, **274**, 869-884.
- X. Li and C. Wang, *J. Mater. Chem. A*, 2013, **1**, 165-182.
- W.-M. Zhang, X.-L. Wu, J.-S. Hu, Y.-G. Guo and L.-J. Wan, *Adv. Funct. Mater.*, 2008, **18**, 3941-3946.
- P. L. Taberna, S. Mitra, P. Poizot, P. Simon and J. M. Tarascon, *Nat Mater.*, 2006, **5**, 567-573.
- P. Poizot, S. Laruelle, S. Grugeon, L. Dupont and J. M. Tarascon, *Nature*, 2000, **407**, 496-499.
- M. V. Reddy, T. Yu, C. H. Sow, Z. X. Shen, C. T. Lim, G. V. Subba Rao and B. V. R. Chowdari, *Adv. Funct. Mater.*, 2007, **17**, 2792-2799.
- Y.-M. Lin, P. R. Abel, A. Heller and C. B. Mullins, *J. Phys. Chem. Lett.*, 2011, **2**, 2885-2891.
- L. Zhang, H. B. Wu, S. Madhavi, H. H. Hng and X. W. Lou, *J. Am. Chem. Soc.*, 2012, **134**, 17388-17391.
- X. Xu, R. Cao, S. Jeong and J. Cho, *Nano Lett.*, 2012, **12**, 4988-4991.
- Y. Zhao, J. Li, Y. Ding and L. Guan, *Chem. Commun.*, 2011, **47**, 7416-7418.
- X. Zhu, Y. Zhu, S. Murali, M. D. Stoller and R. S. Ruoff, *ACS Nano*, 2011, **5**, 3333-3338.
- S. Q. Chen, P. Bao and G. X. Wan, *Nano Energy*, 2013, **2**, 425-434.
- Z. Wang, D. Luan, S. Madhavi, Y. Hu and X. W. Lou, *Energy Environ. Sci.*, 2012, **5**, 5252-5256.
- B. Sun, J. Horvat, H. S. Kim, W.-S. Kim, J. Ahn and G. Wang, *J. Phys. Chem. C*, 2010, **114**, 18753-18761.
- G. Zhou, D.-W. Wang, P.-X. Hou, W. Li, N. Li, C. Liu, F. Li and H.-M. Cheng, *J. Mater. Chem.*, 2012, **22**, 17942-17946.
- Y. Ma, G. Ji and J. Y. Lee, *J. Mater. Chem.*, 2011, **21**, 13009-13014.
- O. Vargas, A. Caballero and J. Morales, *Electrochim Acta*, 2014, **130**, 551-558.
- J. Lin, A.-R. O. Raji, K. Nan, Z. Peng, Z. Yan, E. L. G. Samuel, D. Natelson and J. M. Tour, *Adv. Funct. Mater.*, 2014, **24**, 2044-2048.
- Q. Zhu, F. Tao and Q. Pan, *ACS Appl. Mater. Interfaces*, 2010, **2**, 3141-3146.
- M. Descostes, F. Mercier, N. Thommat, C. Beaucaire and M. Gautier-Soyer, *Appl. Surf. Sci.*, 2000, **165**, 288-302.

- 23 Y. Liu, L. Yu, Y. Hu, C. Guo, F. Zhang and X. Wen Lou, *Nanoscale*, 2012, **4**, 183-187.
- 24 X. L. Jia, Z. Chen, X. Cui, Y. T. Peng, X. L. Wang, G. Wang, F. Wei and Y. F. Lu, *Acs Nano*, 2012, **6**, 9911-9919.
- 25 Y. Z. Wu, P. B. Zhu, M. V. Reddy, B. V. R. Chowdari and S. Ramakrishna, *ACS Appl. Mater. Interfaces*, 2014, **6**, 1951-1958.
- 26 C. He, S. Wu, N. Zhao, C. Shi, E. Liu and J. Li, *ACS Nano*, 2013, **7**, 4459-4469.
- 27 J. Y. Shin, D. Samuelis and J. Maier, *Adv. Funct. Mater.*, 2011, **21**, 3464-3472.
- 28 E. Z. Liu, J. M. Wang, C. S. Shi, N. Q. Zhao, C. N. He, J. J. Li and J. Z. Jiang, *ACS Appl. Mater. Interfaces*, 2014, **6**, 18147-18151.
- 29 X. Wang, L. Qiao, X. Sun, X. Li, D. Hu, Q. Zhang and D. He, *J. Mater. Chem. A*, 2013, **1**, 4173-4176.
- 30 W. Chen, Z. Zhang, W. Bao, Y. Lai, J. Li, Y. Gan and J. Wang, *Electrochim Acta*, 2014, **134**, 293-301.
- 31 W.-J. Yu, P.-X. Hou, F. Li and C. Liu, *J. Mater. Chem.*, 2012, **22**, 13756-13763.
- 32 Y. Shi, B. Guo, S. A. Corr, Q. Shi, Y.-S. Hu, K. R. Heier, L. Chen, R. Seshadri and G. D. Stucky, *Nano Lett.*, 2009, **9**, 4215-4220.
- 33 Z. Wang, J. S. Chen, T. Zhu, S. Madhavi and X. W. Lou, *Chem. Commun.*, 2010, **46**, 6906-6908.
- 34 Y. Yu, C. H. Chen and Y. Shi, *Adv. Mater.*, 2007, **19**, 993-997.
- 35 S.-H. Lee, Y.-H. Kim, R. Deshpande, P. A. Parilla, E. Whitney, D. T. Gillaspie, K. M. Jones, A. H. Mahan, S. Zhang and A. C. Dillon, *Adv. Mater.*, 2008, **20**, 3627-3632.
- 36 H.-X. Zhang, C. Feng, Y.-C. Zhai, K.-L. Jiang, Q.-Q. Li and S.-S. Fan, *Adv. Mater.*, 2009, **21**, 2299-2304.
- 37 C. Comminges, R. Barhdadi, M. Laurent and M. Troupel, *J. Chem. Eng. Data*, 2006, **51**, 680-685.
- 38 T. Kennedy, E. Mullane, H. Geaney, M. Osiak, C. O'Dwyer and K. M. Ryan, *Nano Lett.*, 2014, **14**, 716-723.
- 39 J. Erlebacher, M. J. Aziz, A. Karma, N. Dimitrov and K. Sieradzki, *Nature*, 2001, **410**, 450-453.
- 40 X. H. Liu, S. Huang, S. T. Picraux, J. Li, T. Zhu and J. Y. Huang, *Nano Lett.*, 2011, **11**, 3991-3997.
- 41 P. Balaya, H. Li, L. Kienle and J. Maier, *Adv. Funct. Mater.*, 2003, **13**, 621-625.
- 42 Q. Zhang, T. Peng, D. Zhan and X. Hu, *J Power Sources*, 2014, **250**, 40-49.